Mechanical behavior of highly cross-linked polymer networks and its links to microscopic structure

Debashish Mukherji* and Cameron F. Abrams
Department of Chemical and Biological Engineering, Drexel University, Philadelphia, Pennsylvania 19104, USA
(Received 1 January 2009; published 8 June 2009)

Highly cross-linked polymer (HCP) networks are becoming increasingly important as high-performance adhesives and multifunctional composite materials. Because of their cross-linked molecular architectures, HCPs can be strong but brittle. One key goal in improving the performance of an HCP is to increase toughness without sacrificing strength. Using large scale molecular-dynamics simulation, we compare and characterize the mechanical behavior of two model HCPs under tensile deformation. In the first case, bond angles among any three connected monomers are unconstrained and in the second case we impose harmonic tetrahedral bond angle constraints. We perform a detailed microstructural analysis that establishes a unique correlation between *macroscopic* mechanical behavior and the *microscopic* structure of an HCP. While, in the unconstrained system, strain-hardening behavior is observed that is attributed to the formation of microvoids, the void growth is completely arrested in the constrained system and no strain hardening is observed. Moreover, after the initial strain-hardening phase, the unconstrained system displays the same stress-strain behavior as that of a constrained network. Strain hardening makes the unconstrained system ductile while it retains the same tensile strength as the constrained system. We suggest that bond angle flexibility of cross-linkers might be a possible means to control ductility in an HCP network at a constant cross-linker density. We have also studied the effect of temperature, strain rate, and intermonomer nonbonded interaction strength on the stress-strain behavior. Interestingly at a strong intermonomer nonbonded interaction strength, no strain hardening is observed even in the unconstrained system and fracture sets in at around 1% strain, similar to what is observed in an experimental system such as epoxy and vinyl-ester based thermosets. This indicates that strong nonbonded interactions play a key role in making an HCP strong but brittle.

DOI: 10.1103/PhysRevE.79.061802 PACS number(s): 61.41.+e, 87.15.La, 87.10.Tf

I. INTRODUCTION

Rational design of improved adhesives and composite materials requires the ability to predict, based on molecular structure, properties such as tensile strength, fracture strain, Young's modulus, and strain-hardening modulus, to name a few [1,2]. While attention to such structure-function relationships has been mostly limited to dense systems of linear polymer chains under externally imposed deformation [3–7], more recent interest has focused on the underlying phenomena that govern the mechanical properties of highly cross-linked polymers (HCP) [8–11].

HCPs are three-dimensional networks of covalently connected monomers, and they exhibit a wide range of exotic and unpredictable behavior [10,12–14]. Despite development of HCPs with improved performance, theories linking structure to mechanical properties are limited. This deficiency is partly due to the complex extended molecular structures associated with HCP networks, which are difficult to specify to a desired degree. Therefore, simulations have become a method of choice [9,11,15,16] to ascertain what molecular level mechanisms govern the mechanical behavior of HCP networks. In one of the earliest studies of HCP adhesives, molecular-dynamics (MD) simulation of a generic coarse-grained bead-spring model was used to study the effect of interfacial bond density on mechanical fracture in HCP [9]. In follow-up work, the effect of cross-linker functionality on mechanical properties was investigated [11]. In these studies, initial conditions were manipulated to localize the fracture near the interface, which was achieved by allowing monomers to form fewer bonds near the surface than in the bulk region. More recently, a hybrid model was developed in which coarse-grained beads were cross-linked applying Monte Carlo moves and then inverted into a full atomistic model for MD [16].

An important drawback of many HCPs is a lack of ductility in the glassy state. For example, around 2 GPa of stress is required to fracture an epoxy at an extremely brittle deformation of 1%. Recent understanding suggests that ductility can be achieved in a glassy state epoxy network by reducing the cross-linker density [17]. In general, reducing cross-linker density does enhance energy dissipation by enabling larger degrees of plastic deformation before fracture sets in. However, this reduction in cross-link density greatly sacrifices tensile strength [17,18]. In a recent shorter communication, using MD simulation of a generic model, we have shown that an HCP network can exhibit strain-hardening behavior that makes an HCP network ductile without altering its tensile strength at a constant cross-link density [19]. This behavior was attributed to the formation of microvoids in the sample. The void size distribution followed a functional form well-known from Lennard-Jones (LJ) particle packings [20,21] but was shown to hold an order of magnitude beyond its original domain. It was also shown that voids did not develop for a system with bond angle constraints, and this system also did not strain harden. The purpose of this paper

*debashish.mukherji@drexel.edu

is to present an extended analysis of this HCP strain-hardening behavior and to extend the study of these systems to explain the role of nonbonded attraction in determining material properties. Specifically we consider the effect of degree of bond angle flexibility, temperature, strain rate, and intermonomer nonbonded interaction strength on the mechanical properties of HCP networks. We perform a detailed microstructural analysis that provides a molecular level explanation of several aspects of the mechanical behavior of a model HCP network.

The remainder of the paper is organized as follows: in Sec. II we sketch our methodology. Results for both models are presented in Sec. III, where we first show the stress-strain behavior in Sec. III A. The links between material properties and the microscopic structure of an HCP is shown in Sec. III B. Conclusions are drawn in Sec. IV.

II. METHOD AND MODELS

Our system consists of a 95% cured HCP confined between two crystalline surfaces. For our study, a simple coarse-grained bead-spring model is used [22,23]. The model consists of point-mass beads that are connected to each other with massless springs. The following few aspects of our treatment will be described here: interaction between monomers, surface structure, sample preparation, network formation, and thermostatting.

A. MD method: Langevin dynamics

In this study, we employ regular MD, in which temperature is imposed by coupling a Langevin thermostat [22],

$$m\ddot{\mathbf{r}}_i = -\nabla_i V - \gamma m\dot{\mathbf{r}}_i + \mathbf{\Gamma}_i(t), \tag{1}$$

where V is the total interaction potential and γ is the damping coefficient. A velocity-dependent frictional force and a random force $\mathbf{\Gamma}_i(t)$ are added to the equation of motion. The random force $\mathbf{\Gamma}_i(t)$ satisfies the fluctuation-dissipation theorem

$$\langle \mathbf{\Gamma}_i(t) \cdot \mathbf{\Gamma}_j(t') \rangle = 6mk_B T\gamma\delta_{ij}\delta(t-t'). \tag{2}$$

The equation of motion is integrated with the velocity-Verlet algorithm [24] with a time step $\delta t = 0.005\tau$. The glass transition temperature of confined LJ system is $T_g = 0.5u_0/k_B$ [9,25]. In order to study the temperature dependence of mechanical properties, we varied thermal energy from below T_g (i.e., $0.3u_0/k_B$) to a temperature, $T = 1.1u_0/k_B$, at which system is in a rubbery state.

B. Interparticle potentials

In this model, individual monomers interact with each other via a truncated LJ potential [22],

$$V_{LJ}(r) = \begin{cases} 4u_0\left[\left(\frac{d}{r}\right)^{12} - \left(\frac{d}{r}\right)^{6} - \left(\frac{d}{r_c}\right)^{12} + \left(\frac{d}{r_c}\right)^{6}\right], & \text{for } r < r_c, \\ 0, & \text{elsewhere}, \end{cases} \tag{3}$$

with the cutoff radius, r_c, chosen to be $2.5d$. Here u_0 is the unit of energy and d is the unit of length. The results presented below are expressed in units of the LJ energy u_0, the LJ radius d, and the mass m of individual monomers. This gives unit of time as $\tau = d\sqrt{m/u_0}$. Values representative of hydrocarbons are as follows: $u_0 = 30$ meV, $d = 0.5$ nm, $\tau = 3$ ps, and the unit of pressure is $p_0 = 40$ MPa [25].

Following Stevens [9], we use a bond potential to model breakable covalent bonds that is the sum of purely repulsive Weeks-Chandler-Andersen (WCA) potential,

$$V_{WCA}(r) = \begin{cases} 4u_0\left[\left(\frac{d}{r}\right)^{12} - \left(\frac{d}{r}\right)^{6} + \frac{1}{4}\right], & \text{for } r < 2^{1/6}d, \\ 0, & \text{elsewhere}, \end{cases} \tag{4}$$

and a quartic potential,

$$V_{bond}(r) = \begin{cases} \kappa_4(y-r_1)(y-r_2)y^2 + U_0, & r < 1.5d, \\ U_0, & r \geq 1.5d, \end{cases} \tag{5}$$

where $\kappa_4 = 1434.3u_0/d^4$, $y = r - \Delta r$, $\Delta r = 1.5d$, $r_1 = -0.7411d$, $r_2 = 0$, and $U_0 = 67.2234u_0$ [9]. The precise choice of r_1 gives an effective bond length of $0.97d$ [22]. The cutoff distance $1.5d$ is the maximum extension of the bond, beyond which the bond breaks.

In the case of the constrained system, we also include an additional bond angle potential that enforces a tetrahedral bonding geometry,

$$V_{angle}(\theta_{ijk}) = \kappa_\theta(\theta_{ijk} - \theta_0)^2, \tag{6}$$

where unless stated otherwise $\theta_0 = 1.91$ rad (or 109.45°) and $\kappa_\theta = 0.02u_0/\text{rad}^2$. The angle θ_{ijk} is the effective angle between bond vectors $\mathbf{b}_{ij}$ and $\mathbf{b}_{jk}$.

C. Crystalline confining walls

The system is confined between two walls, each of which consists of two closed packed layers of atoms, mimicking a (111) plane of a face-centered-cubic solid. The atoms of the surface are tethered to their equilibrium sites by a spring with force constant $\kappa = 5000u_0/d^2$. Nearest-neighbor spacing between the substrate atoms is $\delta = 1.209\sigma$ and the area of the surface is expressed as $A = N_s\delta^2\sqrt{3}/2$, where N_s is the number of substrate atoms. The geometry of the substrate is essentially square with a fixed linear dimension $L_x \approx L_y$. Periodic boundary conditions are employed in the plane of the substrate. Normal extension is defined as L_z which is the instantaneous separation between inner surfaces of each walls.

D. Sample preparation

1. Precure warm up

An initial configuration is generated by randomly distributing N monomers within the simulation box $L_x \times L_y \times L_z^o$, where L_z^o is the initial interwall separation. The system is then subjected to a 4000 MD time step warm up stage to remove the bead-bead overlaps using force capping. Specifically, the interparticle WCA forces are adjusted according to

$$F(r_{ij}) = \begin{cases} F^0(r_{ij}), & \text{for } F^0(r_{ij}) < F_c(t) \\ F_c(t), & \text{for } F^0(r_{ij}) \geq F_c(t) \end{cases} . \quad (7)$$

The capping force, $F_c(t)$, follows a linear time dependence,

$$F_c(t) = \frac{(F_{\max} - F_{\min})}{t_{\max}} t, \quad (8)$$

where $F_{\min} = 1u_0/d$ and $F_{\max} = 1500u_0/d$ is the force capping range, and $t_{\max}$ is the duration of the warm up stage.

2. Curing: network formation

After warm up, the simulation enters a curing phase in which particle-particle bonds are allowed to form. A bond between any two particles is allowed to form, provided the following conditions are met:

(i) The distance between particles is $1.3d$ or less.

(ii) Both particles have not yet formed the maximum number of allowed bonds. In our simulations each fluid particle is allowed to form at most four bonds to other fluid particles and an additional four bonds to surface atoms.

(iii) A uniform random number, selected between zero and one, is less than a stipulated bond-formation probability, P_{bond}. In our case P_{bond} is chosen as 10^{-4} to attenuate the rate at which energy enters the system due to the formation of bonds.

(iv) In the case of a constrained system we also include an additional harmonic bond angle potential as soon as the two bonds emanating from a particle is formed. Since our system consists of four functional monomers and the curing is conducted at a very slow rate, the local structure of a network is more or less tetrahedral.

Unless stated otherwise, we set temperature at $1.1u_0/k_B$ during the slow curing stage. A constant compressive pressure, $P_l = 3.5u_0/d^3$, is maintained on the upper wall during the bond formation and subsequent quenching. This small P_l is employed to take additional precaution against void growth, which may occur due to the strong tendency for the system to decrease its volume during curing and quenching [19]. A typical duration of 30 000 MD time steps generates a sample in which 95% of possible $4N/2$ bonds are formed. After curing the sample is quenched down to a desired temperature.

It is important to mention that for a constrained system we do not employ any smooth cutoffs for the angle potentials designed to prevent the occurrence of impulse forces upon forming or breaking of bonds. However, given the value of the angle potential harmonic spring constant we used, such impulse forces are negligible compared to the other conservative forces and they are more or less instantly dissipated by the thermostat.

E. Tensile deformation

A schematic representation of our model is shown in Fig. 1. Tensile deformation is imposed by pulling the upper wall with a constant velocity $\dot{L}_z$ that defines a strain rate of $\dot{\epsilon} = \dot{L}_z/L_z^o$. In a series of simulations the value of $\dot{\epsilon}$ is varied from $2 \times 10^{-4}\tau^{-1}$ to $10^{-3}\tau^{-1}$. In this study, we consider three system sizes $N = 100\,000$, 510 000, and 1 000 000. There is no detectable distinction between the stress-strain plot corresponding to system sizes 510 000 and 1 000 000, and therefore all results in this paper are presented for a system of size 510 000. Results are averages of two or three independent simulations with stochastically independent initial configurations.

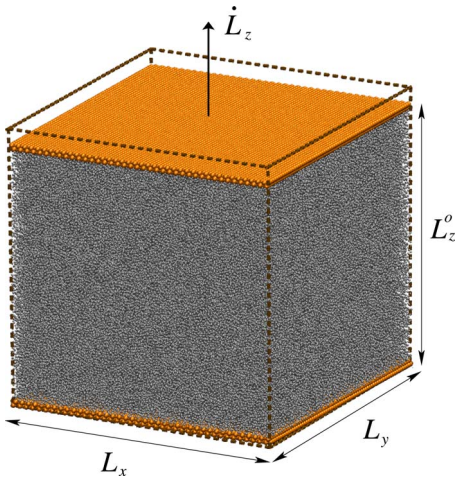

FIG. 1. (Color online) A space-filling representation of a model HCP. Here L_x, L_y, and L_z^o are linear dimensions along x, y, and z directions, respectively. $\dot{L}_z$ is the velocity of upper wall through which the tensile deformation is imposed.

III. RESULTS AND DISCUSSIONS

A. Stress vs strain

1. Strain hardening and the role of bond angle constraints

We plot engineering stress, σ, as a function of engineering strain, $\epsilon = (L_z - L_z^o)/L_z^o$, in Fig. 2. Results are shown for four different bond angle stiffnesses, κ_θ. For $\kappa_\theta = 0$ and 0.001, four regimes are clearly visible: an initial regime $\epsilon \approx 1\%$, where stress increases rapidly with a small network deformation. Above these strains (i.e., $1\% < \epsilon < 15\%$) stress increases nonlinearly with increasing strain. During this stage

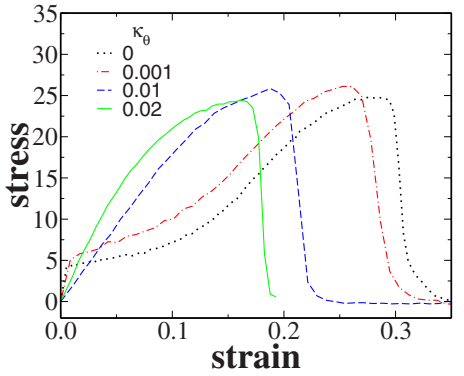

FIG. 2. (Color online) Stress versus strain plot for our model HCP for four different bond angle stiffness, κ_θ. Simulations are carried out at a constant strain rate $\dot{\epsilon} = 2 \times 10^{-4}\tau^{-1}$ and temperature is set to $0.3u_0/k_B$.

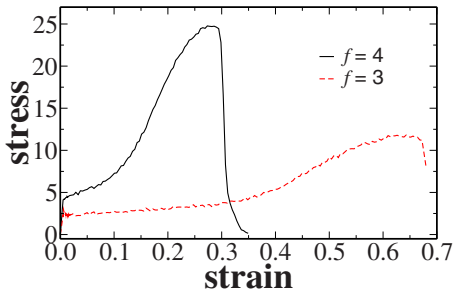

FIG. 3. (Color online) Stress versus strain plot for $\kappa_\theta=0$. Results are shown for two different functionalities $f=4$ and $f=3$. Simulations are carried out at a constant strain rate $\dot{\epsilon}=2\times10^{-4}\tau^{-1}$ and temperature is set to $0.3u_0/k_B$.

no bonds break. However, this initial tensile deformation induces structural rearrangement in the sample which makes the system harder. This behavior is reminiscent of strain hardening in polymer glasses [1,2]. For $\epsilon>15\%$ an irreversible plastic deformation occurs and the first bond breaks around $\epsilon\approx15\%$. Beyond $\epsilon=15\%$, bonds rapidly break leading to total failure of the network as the stress falls to zero. The sample also achieves a tensile strength of about $25u_0/d^3$. For stiff bond angle constraints (i.e., $\kappa_\theta=0.01$ and 0.02) we do not observe strain-hardening behavior.

In general, strain hardening in polymeric systems is associated with necking of the sample, which orients covalent bonds in the direction of the deformation and is known to make the system harder [1,2]. However, due to multiple connectivities of monomers, there is no *a priori* allowance for such behavior in HCP networks. Therefore it is worthwhile to investigate the possible microscopic phenomenon that governs strain hardening in HCPs. In a shorter prior communication [19], we have shown that the strain hardening in HCP can be explained by the formation of microvoids well before the bond breaking sets in. In contrast, void growth is completely arrested in the system with strongly constrained bond angles, as in the case of $\kappa_\theta=0.01$ and 0.02, and thus no strain hardening is observed (see Fig. 2).

It can be appreciated from Fig. 2 that, by changing the bond angle stiffness, κ_θ, we can manipulate the ductility of our model HCP. While recent experiments suggest that the ductility can be enhanced by reducing the number of cross-linkers per unit volume [17], we show that ductility can be enhanced by changing κ_θ, at a constant cross-link density, without compromising tensile strength, σ_t. Furthermore, to test the effect of reducing bond density we have also conducted simulations where the monomers were allowed to form at most three bonds with their neighbor. A comparative plot for two different monomer functionalities, f's, is shown in Fig. 3. As expected, reducing cross-link density enhances ductility by enabling a relatively larger degree of plastic deformation. However, this also reduces σ_t by a factor of two [17,18].

2. Effect of temperature and strain rate

In this section, we study the effect of temperature T and strain rate $\dot{\epsilon}$ on the stress-strain behavior. We first show the temperature dependence of stress-strain behavior for both model HCPs in Fig. 4. Results are shown for four different temperatures. As expected, the stress-strain behavior shows sensitivity to T. For example, the Young's modulus E, which gives the measure of stiffness of a material, is the slope of the Hookean response of stress-strain behavior. In the case of the unconstrained system, calculation of E is somewhat ambiguous considering that we observe an elastic region only at very low strain values, i.e., $\epsilon<1\%$. E nearly doubles when the temperature changes from $1.1u_0/k_B$ to $0.3u_0/k_B$ for an unconstrained system. Furthermore, σ_t changes by about 20%, which is not unexpected given that at a lower temperatures system is more rigid and hence a larger stress is required to fracture the sample. However, there is no significant change in E for the constrained system [see part (b) of Fig. 4] although the tensile behavior is similar to that of an unconstrained system. This suggests that, as expected, at smaller deformations the nonbonded LJ interaction strength controls the mechanical behavior, whereas at larger deformations the breaking of cross-linkers is responsible for the change in mechanical behavior.

We have also conducted simulations for different strain rates $\dot{\epsilon}$'s. Our system shows only a weak strain rate dependence within the values studied here. However, upon increasing $\dot{\epsilon}$ above 10^{-2} we see a clear qualitative deviation from the behavior presented in Fig. 4 (plot not shown). To summarize the results we have plotted Fig. 5, where variation in σ_t as a function of both T and $\dot{\epsilon}$ is shown. σ_t decreases with increasing T and decreasing $\dot{\epsilon}$ [8]. While temperature variation is obvious, the high velocity hardness of a material suggests that at a large $\dot{\epsilon}$ the externally imposed time scale is smaller than the system's internal response time and hence the system appears more rigid.

Although σ_t shows a weak strain rate dependence, the strain to break the sample does not show any noticeable strain rate dependence at a constant temperature. However, strain to break increases with temperature as the system behaves as rubber at higher temperatures (see Fig. 4).

3. Effect of LJ interaction strength

Thus far we have discussed stress-strain behavior and the effects of temperature on the mechanical properties. More-

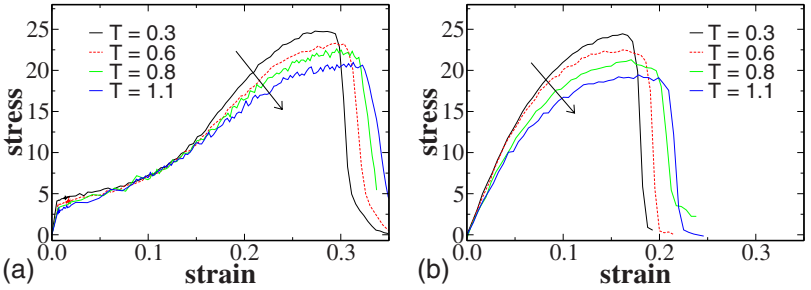

FIG. 4. (Color online) Stress-strain behavior of HCP network for four different temperatures: (a) unconstrained system, and (b) constrained system. Arrows indicate increasing temperature. All simulations are carried out for a strain rate $\dot{\epsilon}=2\times10^{-4}\tau^{-1}$.

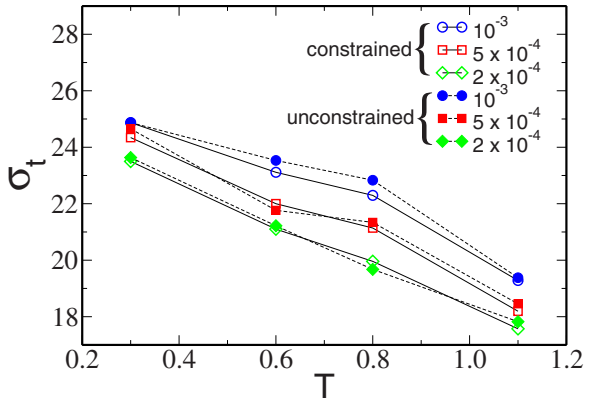

FIG. 5. (Color online) Tensile strength σ_t as a function of temperature, T, for three different strain rates, $\dot{\epsilon}$. Lines are drawn to guide the eye.

over, it is still important to point out that E of an HCP network shows significant sensitivity to temperature. For example, in a glassy state HCP (i.e., for $T=0.3u_0/k_B$) the cross-linkers effectively freeze giving rise to large E. Moreover, for an HCP in its rubbery state (i.e., for $T=1.1u_0/k_B$) one would expect to observe an order-of-magnitude reduction in E. However, we do not observe this trend in our simple coarse-grained model. Therefore to further investigate what controls the mechanical behavior of an HCP network in its glassy state, we study the effect of changing intermonomer nonbonded interaction strengths on the stress-strain behavior. Results are shown in Fig. 6. By increasing nonbonded interaction strength, we observe two distinct features in the case of unconstrained system: (a) the system is less ductile with increased tensile strength and (b) doubling the interaction strength also doubles E at fixed T. Moreover, changing nonbonded interaction does not significantly affect the behavior of a constrained HCP system.

In the case of the unconstrained system, we have also conducted simulations for two more nonbonded interaction strengths, as shown in part (a) of Fig. 6. One interesting result is that for $8.0u_0$ we do not observe any strain hardening and only brittle fracture occurs. Furthermore, we observe fracture at around 1% strain, similar to what is observed in experimental systems such as epoxy and vinyl-ester based thermosets. This indicates that in a real system atoms might be arranged in a way that results in a stronger van der Waals interaction than in a typical liquid, making an HCP network strong but brittle. We still point out that a similar trend is not observed for a constrained system. This insensitivity of stress-strain behavior in a constrained system with LJ interaction strength can only be explained by analyzing the structure of a network, as we do in the next section.

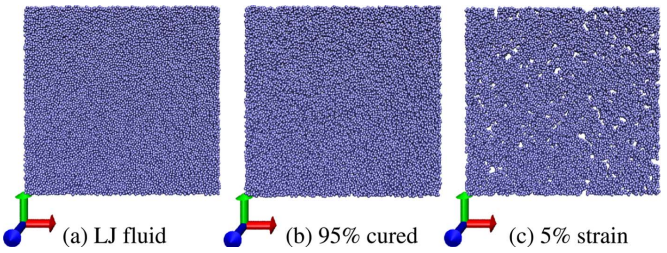

FIG. 7. (Color online) Molecular snapshot at a particular depth to show the lateral distribution of the void along the x-y plane. Three snapshots are drawn for (a) LJ fluid at $\rho=0.93d^{-3}$, (b) 95% cured sample at $\rho=0.94d^{-3}$, and (c) after 5% strain at $\rho=0.87d^{-3}$. Blue arrow represents the $\hat{z}$ direction. Here ρ is density of particle packings. All simulation snapshots are presented for the glassy state HCP.

B. Structural properties

1. Microvoid formation and strain hardening in unconstrained system

Whenever a polymeric system is subjected to an external deformation, the work done is partially dissipated and partially transferred into the conformational changes in polymer chains. Change in polymer conformation is usually attributed to the creation of internal surface area, which results in cracks and crazes [26]. These crazes generally originate near the region of localized tension and thus result in toughening. Our HCP system also shows microvoids (see Fig. 7), which suggests that strain hardening in our model HCP can be explained due to the formation of these microvoids.

One might guess that, whenever a void surface is created, it is associated with broken bonds. However, during the early stage of void formation and growth, no bond breaks in our HCP network.

Formation and growth of void volume is well-known phenomenon in the LJ particle packings [21,27]. It is shown that number density of particle packings, ρ, has an intimate relation to the formation of voids, and voids grow in size with the reduction in ρ. It was also shown that void of a particular large size can only form if the density goes below the so-called "critical density," ρ^*, which was found to be $0.89d^{-3}$ for LJ particle packings [27]. In our simulations we observe similar trend; ρ decreases with increased ϵ due to the z expansion of the simulation box, consistent with the increased

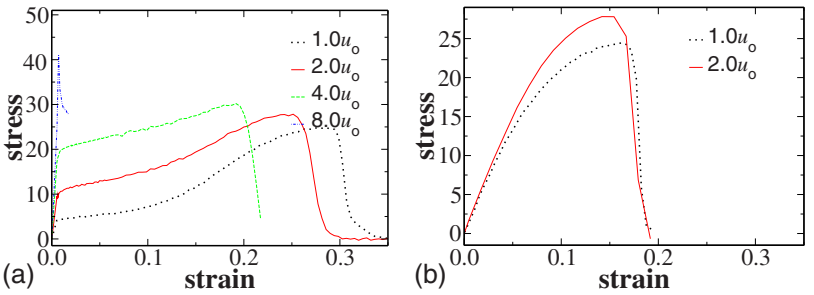

FIG. 6. (Color online) Stress-strain behavior of HCP network for different LJ interaction strengths. Results in (a) corresponds to unconstrained system and (b) for constrained system. All simulations are carried out for a strain rate $\dot{\epsilon}=2\times10^{-4}\tau^{-1}$ and thermal energy is set to $0.3u_0/k_B$. Part (a) also contains graph with intermonomer nonbonded interaction $4.0u_0$ and $8.0u_0$.

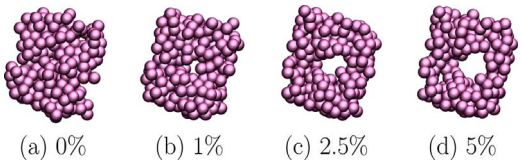

FIG. 8. (Color online) Simulation snapshots of a particular void at various ϵ's. Four snapshots corresponds to: (a) $\epsilon=0\%$ at $\rho=0.94d^{-3}$, (b) $\epsilon=1\%$ at $\rho=0.92d^{-3}$, (c) $\epsilon=2.5\%$ at $\rho=0.90d^{-3}$, and (d) $\epsilon=5\%$ at $\rho=0.87d^{-3}$.

void size with increasing ϵ, as shown in Fig. 8. One would expect to see brittle fracture if most of the void volume was due to the presence of one dominant large void. Moreover, strain hardening is only made possible due to the presence of several smaller voids in the sample [see part (c) of Fig. 7]. Therefore it is important to understand what determines the distribution of void sizes.

A standard method to visualize voids in the system is the analysis of void clusters according to their size. For this purpose, we discretize our simulation box into cubic voxels of linear dimension that varied from $0.4d$ to $0.8d$ depending on the temperature. A voxel is considered to be void space if there is no monomer inside it and also the centroid of a monomer is farther than $d/2$ distance from the box boundary. Empty boxes are clustered into voids according to the rule that any two empty face-sharing voxels must belong to the same void. Subsequently, void size is measured as the number of voxels in a distinct void times volume of a single voxel.

There has been a long history of studying statistical thermodynamics of void space in dense particle packings [20,21,28,29]. Therefore before going into our results, we briefly want to discuss some of the key ingredients of existing theory. In general, there are two main distinctions of the void spaces in LJ particle packings: free volume and cavity volume. While the former gives the measure of a void space in the vicinity of a particle where the parent particle is free to move, the latter gives a void volume where a foreign particle can be accommodated [29]. The probability that a particle has a free volume between v and $v+dv$ can be written as [20,21]

$$f(v)dv = \frac{vP(v)}{\int vP(v)dv}dv \propto v^{\alpha}\exp\left(-\frac{E_p}{k_BT}\right)dv, \qquad (9)$$

where $P(v)dv$ is the probability of finding a cavity between volumes v and $v+dv$, and E_p is size dependent pseudoenergy that scale as v^{ζ}. Here α and ζ are positive fitting parameters. This gives an effective distribution function for the cavity volume [19],

$$P(v) = \frac{n(v)}{\sum_v n(v)} \propto v^{\alpha-1}\exp\left(-\frac{E_p}{k_BT}\right), \qquad (10)$$

where $n(v)$ is number of voids with volume, v. We have plotted this distribution function, $P(v)$, measured directly from the simulations in Fig. 9. It is clearly visible from Fig. 9 that smaller voids are more numerous such that void volume is distributed among as many voids as possible, whereas the probability of observing large voids is small. While the data for $P(v)$ is strain or strain rate independent [19], it does show sensitivity to temperature. Furthermore, we observe that the data can easily be described by Eq. (10) [20,21]. Fitting Eq. (10) to the data in Fig. 9, we find $\alpha=0.32$ and $\zeta=0.27$ for the glassy state HCP. In the other case of $T=0.8u_0/k_B$, the data can be described only by changing ζ to 0.75. Furthermore there are two distinct contributions that constitute Eq. (10). The power-law term, $v^{-2/3}$, is a surface energy contribution and the Boltzmann factor measures the energetic penalty for the creation of a void of size v from a homogeneous chunk of material at a given ρ. We find that this pseudoenergy scales as $v^{0.27}$ for an HCP sample in its glassy state.

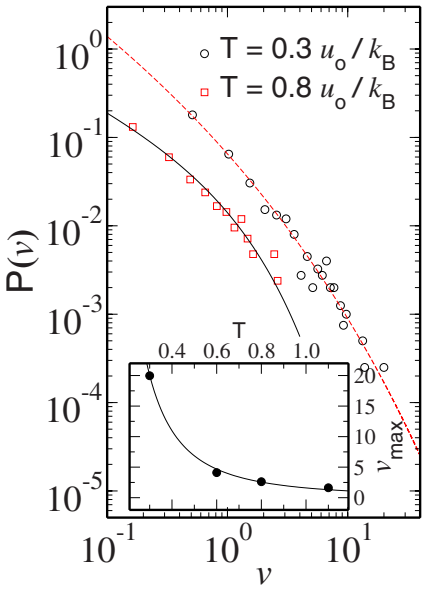

FIG. 9. (Color online) Void size distribution of voids for HCP at two different temperatures. Lines are fits according to Eq. (10) with $\alpha=1/3$ and $\zeta=0.27$ for $T=0.3u_0/k_B$ and 0.75 for $0.8u_0/k_B$, respectively. The inset shows the observation of largest void v_{max} for different temperature. Simulations are carried out at $\dot{\epsilon}=2\times10^{-4}\tau^{-1}$ and after 5% strain at $\rho=0.87d^{-3}$.

From the comparative plot it is evident that the probability of finding large voids is extremely unlikely at large temperatures. Given the Boltzmann-like behavior it is somewhat surprising because a long tail in the distribution function is expected at large temperatures. This counterintuitive behavior can only be explained in terms of ρ^*. Therefore we plot the volume of largest void, v_{max}, obtained in a sample as a function of temperature in the inset of Fig. 9. The size of largest void obtained at $T=1.1u_0/k_B$ is an order-of-magnitude smaller than at $T=0.3u_0/k_B$, suggesting that the ρ^* is temperature dependent and decreases with increasing temperature. Thus it is consistent with the absence of larger voids for $T>0.3u_0/k_B$ at a given density.

We have also investigated void shapes. A quantity that perhaps best describes the shape of a void is its gyration tensor,

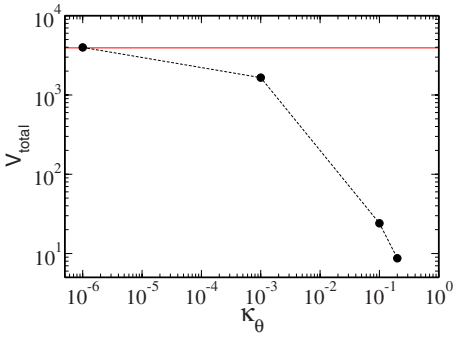

FIG. 10. (Color online) Total void volume, V_{total}, as a function of bond angle stiffness, κ_θ. Solid line represents $V_{\text{total}}(\kappa_\theta \to 0)$.

$$S_{ab} = \frac{1}{N_{\text{voxel}}} \left\langle \sum_{i=1}^{N_{\text{voxel}}} (R_{ia} - \bar{R}_a)(R_{ib} - \bar{R}_b) \right\rangle, \qquad (11)$$

where a and b are Cartesian indices, $\bar{R}_a$ is the center of mass along ath axis, and N_{voxel} is the number of voxels in a particular void. Large voids, for example, of size $v \approx 25d^3$, were predominantly pancake shaped with their smallest axes oriented in the direction of tensile deformation.

The lateral dimensions of the largest void prior to any bond breaking is $6d$, as shown in part (d) of Fig. 8, which is much larger than the maximum extension of the intermonomer bonds (i.e., $1.5d$). Therefore these large voids must be due to the orientation of bonds emanating from the particles sitting at the surface of a void volume. Indeed, by analyzing the bond orientation in the simulation snapshots, we find that almost 95% of the monomers in the periphery of the voids are four coordinated. However, most of the bonds emanating from these peripheral particles are oriented away from the void center. Thus increasing void size with ϵ is due to the disruption of nonbonded interaction between pairs of monomers. This explains why we observe large voids without breaking any bonds. Upon increasing strain above 15%, microcracks propagate in the lateral direction due to bond breaking near lateral periphery of voids, leading ultimately to fracture.

The specific spatial distribution of the monomers is only made possible because bonds are allowed arbitrary orientation so long as particles do not overlap. Therefore, by engaging these voids so that void growth becomes completely arrested, the so-called microvoid based strain hardening should disappear. In our constrained system, the tetrahedral geometry apparently completely arrests the void growth as shown in Fig. 10. It is important to mention that the observed void volume for $\kappa_\theta = 0.01$ and 0.02 is predominantly due to presence of small fraction of monomers that form two or three bonds.

2. Fracture snapshots

It has been discussed that the stress-strain behavior shows a weak strain rate dependence. However, besides having an effect on the tensile strength and failure strain, the effect of the strain rate is seen in the depth at which fracture occurs.

The fracture region is clearly visible from the snapshots of these simulations (Figs. 11 and 12). For $\dot{\epsilon} = 2 \times 10^{-4}\tau^{-1}$, we always observe bulk (or cohesive) fracture, whereas, for higher strain rates, fracture is usually localized within $15d - 20d$ from the upper surface. In our models, the bulk system is more homogeneous and bond density is higher in the bulk region. Therefore, with higher $\dot{\epsilon}$'s the system fractures near the interface. It is important to point out that adhesive fracture always occurs near the upper wall, yet bond density is similar near both walls. Therefore, it is likely that stress is being produced near the upper wall at a rate faster than it can diffuse downward through the sample. Moreover, at a very slow $\dot{\epsilon}$, stress propagation throughout the sample gives rise to a completely cohesive failure.

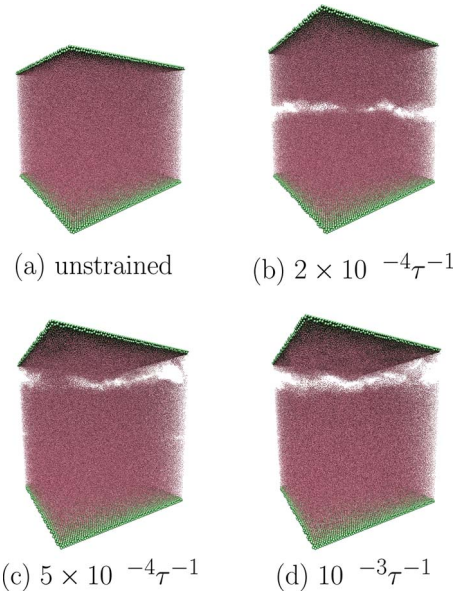

FIG. 11. (Color online) Simulation snapshots demonstrating the tensile failure in a constrained system at different strain rates, $\dot{\epsilon}$. Four snapshots corresponds to: (a) initial sample, (b) for $\dot{\epsilon} = 2 \times 10^{-4}\tau^{-1}$, (c) $\dot{\epsilon} = 5 \times 10^{-4}\tau^{-1}$, and (d) $\dot{\epsilon} = 10^{-3}\tau^{-1}$. All simulations were carried out at a thermal energy $0.3u_0/k_B$.

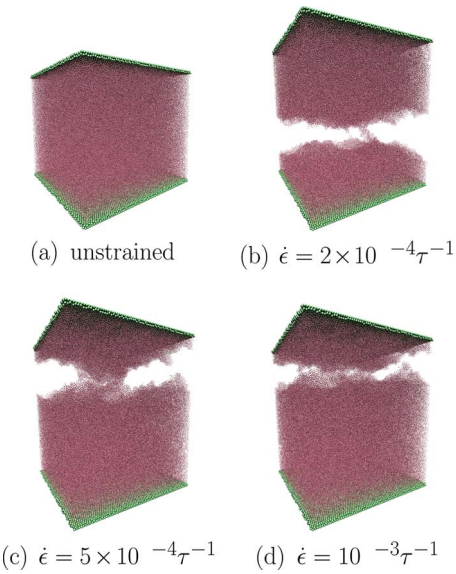

FIG. 12. (Color online) Same as Fig. 11, however for an unconstrained system.

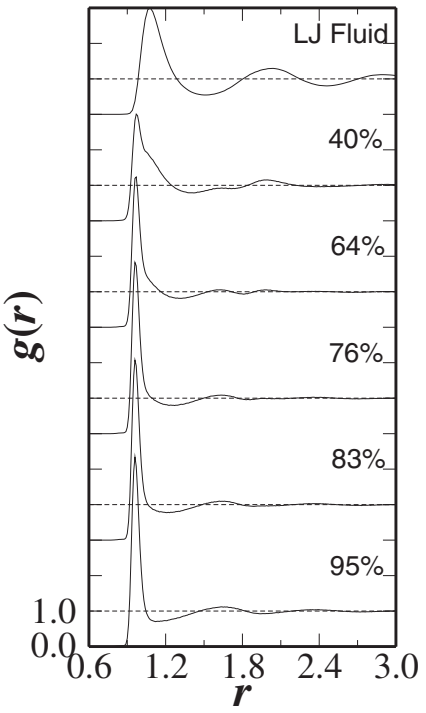

FIG. 13. Radial distribution function, $g(r)$, for a constrained system. Different plots correspond to structure during various curing stages as mentioned in the caption. For comparison we have also drawn $g(r)$ for a simple LJ fluid.

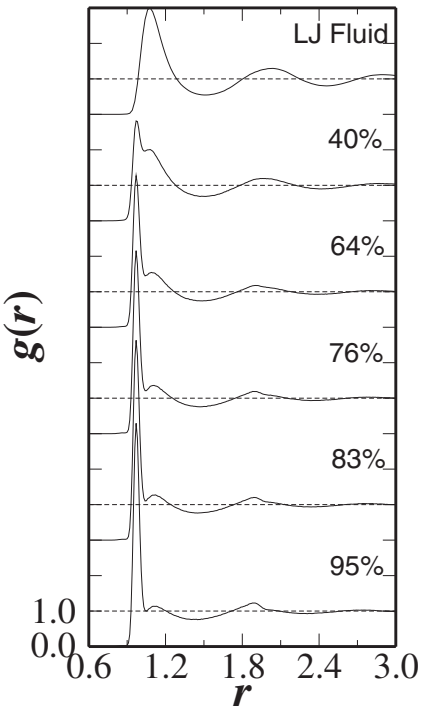

FIG. 14. Same as Fig. 13, however for an unconstrained system.

In a neat HCP, as those in this study, $\dot{\epsilon}$ does not significantly affect the stress-strain behavior and only a weak $\dot{\epsilon}$ dependence is observed. However, $\dot{\epsilon}$ does significantly affect the mechanical behavior of an alloy where linear chains are added to the HCP network. In a recent work, we have shown that for $\dot{\epsilon}=2\times10^{-4}\tau^{-1}$ we can still observe an adhesive failure if the concentration of linear chain is large such that their presence act as a barrier for the stress propagation. More specifically cohesive failure occurs for low linear-chain concentration and an adhesive failure happens for large concentration. This transition gives rise to an anomalous behavior of ductility in an alloy as a function of linear-chain concentration [30].

3. Glassy structure and its role in material properties

In Fig. 6 we have shown that changing intermonomer nonbonded interaction strength does not significantly affect the stress-strain behavior in a constrained HCP system. So, to explain the insensitivity of stress-strain behavior in the constrained system with u_0, we examine the microstructure of HCP networks via the monomer-monomer radial distribution functions, $g(r)$. Figure 13 shows $g(r)$ for a constrained system during various percentage curing. For comparison, Fig. 13 also shows $g(r)$ of a simple LJ fluid, which has a peak at a distance comparable to minima of LJ potential (i.e., $r=2^{1/6}d$). The data clearly show a strong structural rearrangement as the system cures. Several distinct features are clearly visible: (a) first peak shift toward a lower r value with respect to the LJ fluid. This is due to the stipulated cross-link bond length $0.97d$, and with increasing percent cure, particles start accumulating at this distance. (b) Once the system attains a 40% cure there are virtually no visible peaks beyond a distance of $1.8d$, indicating a lack of long-range ordering in the sample. (c) Due to the influence of the additional bonding constraint, individual monomers are nearly frozen near their equilibrium positions and thus exhibit very little thermal motion, which is indicated by the reduced peak width with increasing percent cure. As the stress-strain behavior is different in both systems, one may therefore expect to see different structural behavior in our unconstrained system of HCP. The $g(r)$ for an unconstrained system is plotted in Fig. 14. Similar to Fig. 13, here also we observe a peak at the bond length $0.97d$. Moreover, unconstrained system shows a long-range ordering, similar to that of a LJ fluid, even after the system attains a 95% cure, which is indicated

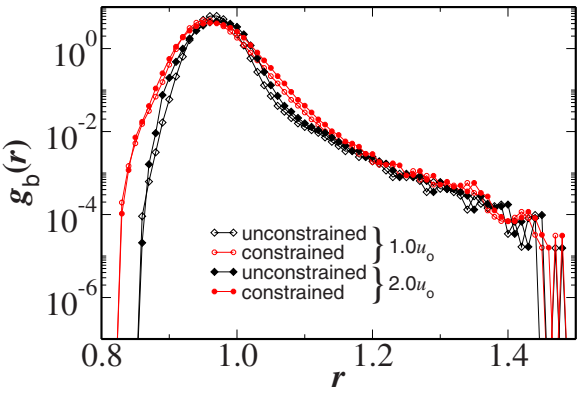

FIG. 15. (Color online) Radial distribution function between bonded monomers, $g_b(r)$. Comparative plots are shown for both HCP systems and for two different LJ interaction strengths.

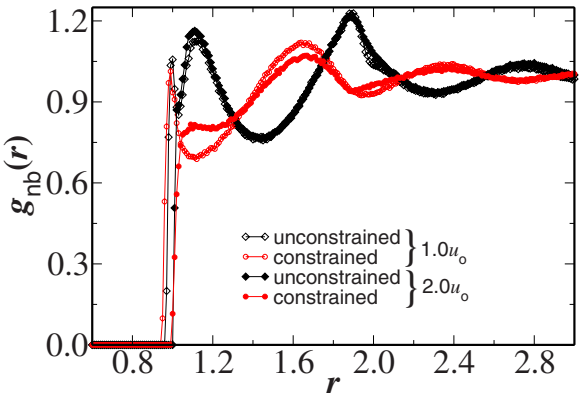

FIG. 16. (Color online) Radial distribution function between nonbonded monomers, $g_{nb}(r)$. Comparative plots are shown for both HCP systems.

by the peak at around $2.0d$, which also coincides with the peak of a LJ fluid.

In order to perform a detailed microstructural analysis we separate $g(r)$ into its bonded, $g_b(r)$, and nonbonded, $g_{nb}(r)$, contributions. Figure 15 shows radial distribution function between bonded monomers, $g_b(r)$. As expected the coordination number, $\rho\int 4\pi r^2 g_b(r)dr$, is around 3.96 for all the cases shown in the Fig. 15, which is consistent with four functional monomers in our HCP network. In Fig. 16, we have shown radial distribution function between nonbonded monomers, $g_{nb}(r)$. It can be appreciated from the plot that for an unconstrained system the structure is predominantly the same irrespective of the nonbonded LJ interaction strength. Hence, doubling interaction strength also doubles the material response, as observed in part (a) of Fig. 6. Moreover, in a constrained system the microscopic structure shows a strong dependence on the nonbonded LJ interaction strength. More specifically for a $2.0u_0$ interaction strength, a larger number of particles accumulate near the LJ equilibrium distance of $2^{1/6}d$, as shown in Fig. 16. This indicates that, with increasing nonbonded LJ interaction strength, particles pack near the bottom of the potential-energy well where net forces on particles are relatively small at low strains. This is consistent with the insensitivity of stress-strain behavior with nonbonded LJ interaction strength for a constrained system [see part (b) of Fig. 6]. That is, increasing u_0 leads to better packing.

IV. CONCLUSIONS

We used MD simulations to compare and characterize the mechanical properties of the two models of highly cross-linked polymer networks. In one model we introduce bond angle constraints such that four functional monomers can form a network with local tetrahedral geometry and in the other case we investigate the simple system where no bond angle constraint was applied. We find that an unconstrained system strain hardens due to spontaneous formation of microvoids. Void size distributions follow a well-known functional form from equilibrium LJ particle packings. In constrained systems, void growth is completely arrested, and this prevents strain hardening. Although the two models are geometrically distinct, their strained network appears to be insensitive to the initially formed structure. Strain hardening makes an unconstrained network more ductile. Flexible cross-linkers may be a possible route to incorporate ductility in an HCP sample without sacrificing tensile strength.

We have also studied the effect of temperature, strain rate, and LJ interaction strength on quantities such as tensile strength and Young's modulus. We explain the observation that a constrained network shows remarkably little sensitivity to the LJ interaction strength. A structural analysis revealed that the LJ interaction between monomers is arrested to its first nearest-neighbor shell, which reduces the net force acting at low strains even though the LJ interaction strength increases. At a very strong intermonomer nonbonded interaction strength, fracture sets in at around 1% strain in an unconstrained system, similar to those observed in an experimental system. This demonstrates that strong nonbonded interactions play a key role for making an HCP strong but brittle.

ACKNOWLEDGMENTS

Financial support from the U.S. Army Research Laboratory through Grant Nos. W911NF-06-2-0013 and W911NF-07-1-0301, and the ACS Petroleum Research Fund Contract No. 42368-G7 is gratefully acknowledged. Snapshots in this paper are rendered using VMD [31].

[1] L. R. G. Treloar, *The Physics of Rubber Elasticity* (Clarendon, Oxford, 1975).
[2] *The Physics of Glassy Polymers*, edited by R. N. Haward and R. J. Young (Chapman and Hall, London, 1997).
[3] A. Baljon and M. O. Robbins, Science **271**, 482 (1996).
[4] R. Everaers and K. Kremer, J. Mol. Model. **2**, 293 (1996).
[5] T. Hölzl, H. L. Trautenberg, and D. Göritz, Phys. Rev. Lett. **79**, 2293 (1997).
[6] S. W. Sides, G. S. Grest, and M. J. Stevens, Phys. Rev. E **64**, 050802(R) (2001).
[7] R. S. Hoy and M. O. Robbins, Phys. Rev. Lett. **99**, 117801 (2007).
[8] M. Miwa and N. Horiba, J. Mater. Sci. **28**, 6741 (1993).
[9] M. J. Stevens, Macromolecules **34**, 2710 (2001).
[10] X. Chen, F. Wudl, A. K. Mal, H. Shen, and S. R. Nutt, Macromolecules **36**, 1802 (2003).
[11] M. Tsige and M. J. Stevens, Macromolecules **37**, 630 (2004).
[12] S. R. White, N. R. Sottos, P. H. Geubelle, J. S. Moore, M. R. Kessler, S. R. Sriram, E. N. Brown, and S. Viswanathan, Nature (London) **409**, 794 (2001).
[13] X. X. Chen, M. A. Dam, K. Ono, A. Mal, H. B. Shen, S. R. Nutt, K. Sheran, and F. Wudl, Science **295**, 1698 (2002).

[14] K. S. Toohey, N. R. Sottos, J. A. Lewis, J. S. Moore, and S. R. White, Nature Mater. **6**, 581 (2007).
[15] M. J. Stevens, Macromolecules **34**, 1411 (2001).
[16] P. V. Komarov, C. Yu-Tsung, C. Shih-Ming, P. G. Khalatur, and P. Reineker, Macromolecules **40**, 8104 (2007).
[17] J. Jang, C. K. Ullal, T. Choi, M. C. Lemieux, V. V. Tsukruk, and E. L. Thomas, Adv. Mater. **18**, 2123 (2006).
[18] M. C. M. van der Saden and H. E. H. Meijer, Polymer **34**, 5063 (1993).
[19] D. Mukherji and C. F. Abrams, Phys. Rev. E **78**, 050801(R) (2008).
[20] W. G. Hoover, N. E. Hoover, and K. Hanson, J. Chem. Phys. **70**, 1837 (1979).
[21] S. Sastry, T. M. Truskett, P. G. Debenedetti, S. Torquato, and F. H. Stillinger, Mol. Phys. **95**, 289 (1998).
[22] K. Kremer and G. S. Grest, J. Chem. Phys. **92**, 5057 (1990).
[23] M. Kröger, Phys. Rep. **390**, 453 (2004).
[24] W. C. Swope, H. C. Anderson, P. H. Berens, and K. R. Wilson, J. Chem. Phys. **76**, 637 (1982).
[25] D. Mukherji and M. H. Müser, Macromolecules **40**, 1754 (2007).
[26] J. Rottler, S. Barsky, and M. O. Robbins, Phys. Rev. Lett. **89**, 148304 (2002).
[27] S. Sastry, P. G. Debenedetti, and F. H. Stillinger, Phys. Rev. E **56**, 5533 (1997).
[28] J. L. Meijering, Philips Res. Rep. **8**, 270 (1953).
[29] R. J. Speedy and H. Reiss, Mol. Phys. **72**, 999 (1991).
[30] D. Mukherji and C. F. Abrams, Phys. Chem. Chem. Phys. **11**, 2113 (2009).
[31] W. Humphrey, A. Dalke, and K. Schulten, J. Mol. Graphics **14**, 33 (1996).